Atmospheric Environment 292 (2023) 119429

Contents lists available at ScienceDirect

Atmospheric Environment

journal homepage: www.elsevier.com/locate/atmosenv

Assessing mass balance-based inverse modeling methods via a pseudo-observation test to constrain NO_x emissions over South Korea

Jeonghyeok Mun [a,b], Yunsoo Choi [c], Wonbae Jeon [b,d,*], Hwa Woon Lee [d], Cheol-Hee Kim [d,e], Soon-Young Park [e], Juseon Bak [e], Jia Jung [f], Inbo Oh [g], Jaehyeong Park [a], Dongjin Kim [a,b]

[a] Division of Earth Environmental System, Pusan National University, Busan, 46241, South Korea
[b] BK21 School of Earth and Environmental System, Pusan National University, Busan, 46241, South Korea
[c] Department of Earth and Atmospheric Sciences, University of Houston, Houston, TX, 77204, USA
[d] Department of Atmospheric Sciences, Pusan National University, Busan, 46241, South Korea
[e] Institute of Environmental Studies, Pusan National University, Busan, 46241, South Korea
[f] Atmospheric Sciences and Global Change Division, Pacific Northwest National Laboratory, Richland, WA, USA
[g] Environmental Health Center, University of Ulsan College of Medicine, Ulsan, 44033, Republic of Korea

HIGHLIGHTS

- Mass balance–based inverse modeling was applied to constrain NO_x emissions.
- Iterative finite difference mass balance method is the most effective method in constraining NO_x emissions in South Korea.
- The highest efficiencies in constraining NO_x emissions using the mass balance-based method are achieved in summer.
- Inverse modeling results differ according to the seasons, the modeling resolutions, and the regridding methods.

GRAPHICAL ABSTRACT

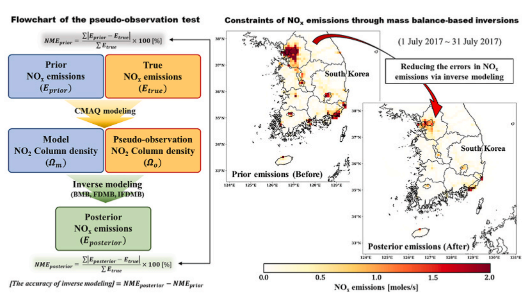

ARTICLE INFO

Keywords:
NO_x emissions
Inverse modeling
IFDMB
Pseudo-observation test
CMAQ
South Korea

ABSTRACT

Using the mass balance-based inverse modeling method, this study constrains NO_x emissions and then examines the optimization of inverse modeling conditions via a pseudo-observation test for South Korea, a country with complex topography. We apply the following mass balance-based inverse modeling methods: basic mass balance (BMB), finite difference mass balance (FDMB), and iterative finite difference mass balance (IFDMB). We perform a numerical simulation of air quality using the Community Multi-scale Air Quality (CMAQ) model to calculate the NO_2 column density required for the inverse modeling. Then we conduct a pseudo-observation test according to the season, the modeling resolution, and the regridding methodology of satellite observational data to identify various conditions while applying inverse modeling for South Korea. Comparing the inverse modeling results from the BMB, FDMB, and IFDMB methods, we find IFDMB the most effective method for constraining NO_x emissions in the South Korean region since it minimizes the smearing effect (i.e., transport-induced errors) through iterative calculations. Our findings show that the accuracy of the constrained NO_x emissions using mass balance-based inversions in South Korea is the highest in the summer season, in which the lowest smearing effect occurs, and the most efficient resolution for the inverse modeling of the region is 9 km. In addition, the results of inverse modeling differ depending on the regridding method, suggesting that the use of a regridding method

* Corresponding author. Department of Atmospheric Sciences, Pusan National University, Busan, 46241, South Korea.
E-mail address: wbjeon@pusan.ac.kr (W. Jeon).

https://doi.org/10.1016/j.atmosenv.2022.119429
Received 21 July 2022; Received in revised form 6 October 2022; Accepted 7 October 2022
Available online 11 October 2022
1352-2310/

suitable for satellite observational data and the modeling resolution is important. This study uses pseudo observations, not actual observations; we expect that in the future, inversions will be applied to inverse modeling studies based on actual satellite data.

1. Introduction

NO_x ($NO + NO_2$) is a key pollutant in terms of atmospheric chemistry as it contributes significantly to the production and loss of tropospheric ozone (O_3) and the production of nitrates or secondary organic aerosols (Crutzen, 1979; Sarrafzadeh et al., 2016; Qu et al., 2017; Liu et al., 2019). Compared to O_3 concentrations in the United States and Europe, those in China and South Korea have recently increased at a rapid pace. In particular, South Korea has experienced greater increases than other regions, signaling an urgent need to identify the scientific causes of this phenomenon (Kim et al., 2018; Lee et al., 2020).

One tool that researchers have used for identifying the scientific causes of high levels of pollution is the chemical transport model (CTM), which simulates past and present air pollution cases (Hu et al., 2016). A significant number of CTM-based O_3 studies in South Korea have adopted the Community Multiscale Air Quality (CMAQ) model (Itahashi et al., 2013; Han et al., 2015; Bae et al., 2018). The accuracy of the results of a CMAQ air quality simulation can be determined by meteorological input data (Jeon et al., 2015; Jeong et al., 2016), emissions (Kurokawa et al., 2009; Souri et al., 2016; Jung et al., 2022), and chemical reaction mechanisms (Kitayama et al., 2019; Appel et al., 2021). The simulation of O_3, the secondary product, requires the accurate emissions data of precursors. Therefore, the accurate calculation of NO_x emissions is essential for analyzing O_3 levels in South Korea. As NO_x emission sources such as industry, road traffic, and shipping are diverse, the acquisition of precise information on the spatial distribution of emission sources is crucial (Lawrence and Crutzen, 1999; Leue et al., 2001).

NO_x emission inventories for air quality modeling have been estimated using a bottom-up method (Tang et al., 2013), which uses factors related to fuel consumption and processes for each emission source to estimate emissions. Errors in the spatial distribution are caused by the omission of unidentifiable emission sources (Martin et al., 2003; Streets et al., 2003; Gu et al., 2016). To reduce the uncertainties in the emissions calculated by the bottom-up method, several studies have used a top-down inverse modeling technique (Zhang et al., 2009; Zhao and Wang, 2009; Lin et al., 2012). This approach estimates variables in the model that cannot be directly measured, such as emissions (Gilliland and Abbitt, 2001). It is possible to create top-down NO_x emission inventories optimized for air quality modeling by minimizing the difference between NO_2 concentrations found by the model and observations via inverse modeling (Napelenok et al., 2008; Cheng et al., 2021). A number of recent studies using the bottom-up approach via inverse modeling have focused on correcting uncertainties in the emission inventory. Representative inverse modeling methods are the Bayesian inverse method (Souri et al., 2016, 2020, 2021; Jung et al., 2022), four-dimensional variational data assimilation (4D-Var) (Kurokawa et al., 2009; Qu et al., 2017, 2019a, 2019b; Zhang et al., 2018; Chen et al., 2021), and the mass balance method (Martin et al., 2003; Lamsal et al., 2011; Cooper et al., 2017; Li et al., 2019).

Mass balance-based inverse modeling is a technique estimating corresponding surface emissions via differences in satellite observations and modeling results for short-lived species (Martin et al., 2003; Pamler et al., 2003). Cooper et al. (2017) used mass balance-based inverse modeling techniques such as basic mass balance (BMB), finite difference mass balance (FDMB), and iterative finite difference mass balance (IFDMB), and constructed a pseudo-observation test to make comparisons with the method using 4D-Var. The pseudo-observation test was ideal for evaluating the performance of inverse modeling systems (Napelenok et al., 2008; Cooper et al., 2017; Qu et al., 2017, 2019; Li et al., 2019). Results of the pseudo-observation test by Cooper et al. (2017) showed that among the mass balance-based inverse modeling methods, the IFDMB method showed similar NO_x emission constraints to those of the more complicated 4D-Var method, which uses more computational resources, suggesting that the IFDMB method is the most effective method. In a study of emissions in North America, Li et al. (2019) used the IFDMB method to constrain NH_3 emissions during each season at a regional scale resolution of the model (i.e., $2^\circ \times 2.5^\circ$ and $0.25^\circ \times 0.3125^\circ$) and showed that the distribution of average NH_3 concentrations varied according to the seasonal characteristics of meteorological factors and the resolution of the model. As the results of mass balance-based inverse modeling differ depending on the transport patterns of pollutants, meteorological conditions that directly and indirectly influence the transport of pollutants affect modeling. Meanwhile, South Korea, a small area surrounded by three seas, has a mountainous topography occupying 70% of the total area. Therefore, high-resolution modeling is essential for a detailed air quality analysis of the regions of South Korea (Bae et al., 2020; Jeong et al., 2020). Currently, research on inverse modeling at a high spatial resolution in South Korea is inadequate.

Thus, to examine inverse modeling conditions optimized for South Korea, this study uses mass balance-based inverse models, including BMB, FDMB, and IFDMB, to constrain NO_x emissions by conducting a pseudo-observation test prior to the application of these models to satellite observation data. The pseudo-observation tests are based on seasons, the resolutions of the models, and grids from the pseudo-ozone monitoring instrument (pseudo-OMI) data. Comparing emission errors before and after modeling, we evaluate the accuracy of inverse modeling. Then we suggest various conditions that one must account for when using satellite observation data such as the OMI, the TROPospheric Monitoring Instrument (TROPOMI), and the geostationary environment monitoring spectrometer (GEMS) in the inverse modeling of South Korea.

2. Data and methodology

2.1. The modeling system and observations

In this study, we used the CMAQ model (v5.3.2) (Appel et al., 2021), a three-dimensional photochemical model developed by the U.S. Environmental Protection Agency (EPA), for air quality numerical simulation. We employed the Weather Research and Forecasting model (WRF, v4.1.1) (Skamarock et al., 2019), a mesoscale meteorological model, to produce a meteorological input field for the CMAQ modeling through the Meteorology Chemistry Interface Processor (MCIP, v5.1). We used ERA5 reanalysis data ($0.25^\circ \times 0.25^\circ$) provided by the European Centre for Medium-range Weather Forecasts (ECMWF) as initial input data for the WRF model. We also applied grid nudging, a method for the optimization of meteorological fields through data assimilation based on initial input data, to obtain more accurate results from the meteorological numerical simulation (Jeon et al., 2015). In addition, meteorological conditions in South Korea vary based on changes in the sea surface temperature (SST) because of the geographical conditions of South Korea (surrounded by three seas). Therefore, when we conducted WRF numerical modeling, we used SST data produced by the UK Met Office's Operational Sea surface Temperature and sea-Ice Analysis (OSTIA) because they are similar to the spatio-temporal distribution of SST near the Korean Peninsula (Xie et al., 2008; Lee et al., 2010; Mun et al., 2017). Emission data from the Mosaic Asian anthropogenic emission inventory (MIX) 2010 (Li et al., 2017) and Clean Air Policy

Support System (CAPSS) 2016/2017 (National Institute of Environmental Research, 2019) were utilized as anthropogenic emission input data for the CMAQ modeling. We used Carbon Bond 6 version 3 (CB6r3) and AERO7 as the chemical mechanisms of the gas and aerosol phases, respectively.

This study consists of two CMAQ modeling domains (Fig. 1). We set the upper domain (D1) to a 27 km horizontal resolution covering East Asia in order to account for the phenomenon of transported pollutants discharged from East Asia to South Korea. Based on the results of D1 modeling, we calculated the initial and boundary fields for the smaller domain, the lower domain (D2), which constituted the study area, South Korea. To identify the effects of inverse modeling, we conducted modeling at resolutions of 27 km (22 × 22), 9 km (66 × 66), and 3 km (198 × 198). To analyze the seasonal difference of inverse modeling, we numerically simulated one month per season: January in the winter, April in the spring, July in the summer, and October in the autumn of 2017. Detailed settings that we applied to the meteorological and air quality models appear in Tables 1 and 2.

To verify the meteorological numerical simulations in this study, we use observational data of surface temperature and wind speed at 95 sites of the Automated Surface Observing Systems (ASOS) in South Korea (Fig. 1). We then compared the seasonal results of the WRF simulations and ground observational data within South Korea to confirm whether the model-simulated meteorological fields based on the seasons were close to those of observations.

2.2. Inverse modeling methods

Inverse modeling derives quantitative constraints on the emissions of corresponding pollutants by accounting for transport and chemical processes based on observational data (Souri et al., 2016). Using NO_2 column density data, this study constrains NO_x emissions via the mass balance-based inverse modeling methodologies (i.e., BMB, FDMB, and IFDMB) suggested by Cooper et al. (2017).

2.2.1. The basic mass balance method

The BMB method estimates NO_x emissions using a simple linear relationship (Eq. (1)). The BMB assumes a linear relationship between

Table 1
Detailed configurations of the Weather Research and Forecasting (WRF) simulation.

WRF	Domain 01 (D1)	Domain 02 (D2)
Horizontal resolution (Number of grids)	27 km (150 × 135)	27 km (35 × 35) 9 km (79 × 79) 3 km (211 × 211)
Vertical layers	15 Layers	
Microphysics option	WSM 3–class simple ice scheme	
Radiation option	Rapid radiative transfer model scheme (longwave) Dudhia scheme (shortwave)	
Surface layer option	Revised mesoscale model 5 Monin–Obukhov scheme (Jimenez)	
Land surface option	Unified Noah land-surface model	
Planetary boundary layer option	Yonsei University scheme	
Cumulus option	Kain–Fritsch (new Eta) scheme	
Initial data	ERA5 (0.25° × 0.25°)	
Simulation period	December 30, 2016, 00 UTC–February 2, 2017, 00 UTC (Winter) March 30, 2017, 00 UTC–May 2, 2017, 00 UTC (Spring) June 29, 2017, 00 UTC–August 2, 2017, 00 UTC (Summer) September 29, 2017, 00 UTC–November 2, 2017, 00 UTC (Fall)	

the observed NO_2 column density ($\boldsymbol{\Omega_o}$) in the troposphere and surface NO_x emissions (E_t) based on the high ratio of NO_2/NO_x and the short lifetime of NO_x (~1 day) within the boundary layer (Martin et al., 2003; Qu et al., 2017; Jung et al., 2022). In Eq. (1), the linear coefficient ($\boldsymbol{\alpha}$) is the ratio between prior NO_x emissions ($\mathbf{E}_a$) and NO_2 column density ($\boldsymbol{\Omega_a}$). The BMB method, the simplest mass balance method, can be applied quickly using a concise algorithm. However, as it is assumed that the NO_x emissions in one grid affect only the NO_2 concentrations of the corresponding grid, the effect of NO_2 transported from another grid is not taken into account.

$$E_t = \boldsymbol{\alpha}\boldsymbol{\Omega}_o, \boldsymbol{\alpha} = \frac{\mathbf{E}_a}{\boldsymbol{\Omega}_a} \quad \text{(Eq. 1)}$$

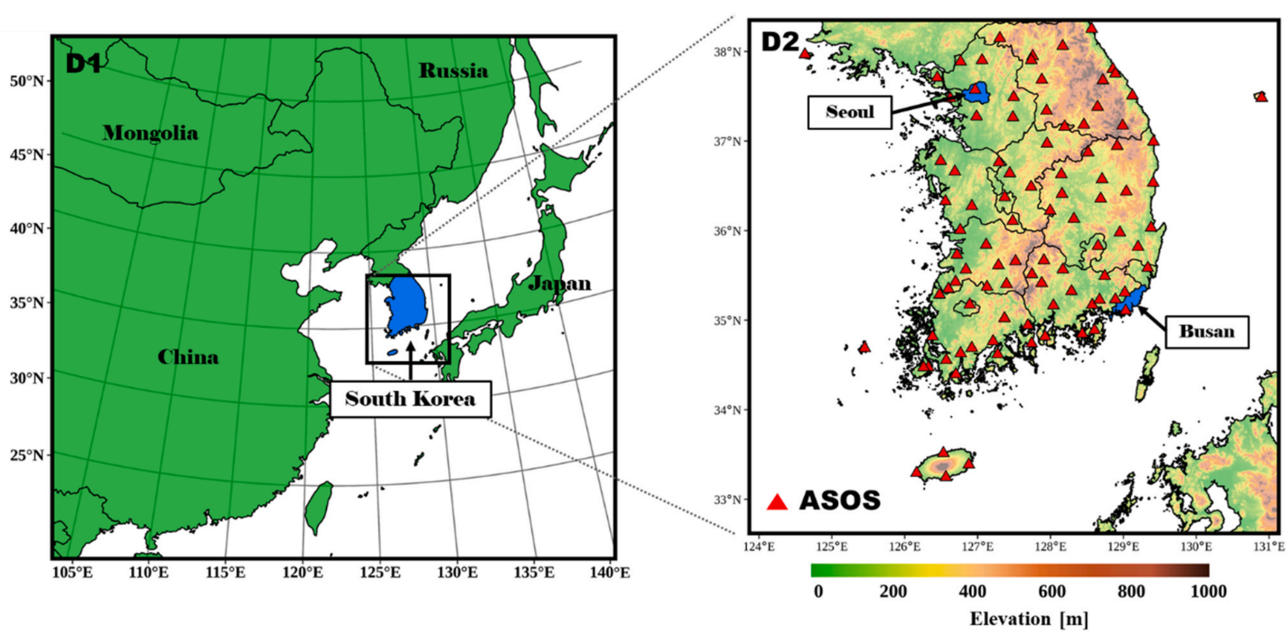

Fig. 1. The numerical simulation domain of the weather research and forecasting (WRF) and community multi-scale air quality (CMAQ) models and the distribution of automated surface observing systems (ASOS) sites within South Korea (red triangles). (For interpretation of the references to colour in this figure legend, the reader is referred to the Web version of this article.)

Table 2
Detailed configurations of the Community Multiscale Air Quality (CMAQ) simulation.

CMAQ	Domain 01 (D1)	Domain 02 (D2)
Horizontal resolution (Number of grids)	27 km (137 × 122)	27 km (22 × 22) 9 km (66 × 66) 3 km (198 × 198)
Vertical layers	15 Layers	
Emission	MIX emission inventory 2010 + CAPSS 2016	
Chemical mechanism	Cb6r3_ae7_aq	
Simulation period	January 1, 2017, 00 UTC–January 31, 2017, 23 UTC (Winter) April 1, 2017, 00 UTC–April 30, 2017, 23 UTC (Spring) July 1, 2017, 00 UTC–July 31, 2017, 23 UTC (Summer) October 1, 2017, 00 UTC–October 31, 2017, 23 UTC (Fall)	

Table 3
Results of the statistical verification of temperature and wind speed simulated by the weather research and forecasting (WRF) model (27 km resolution).

Temp. [°C]	OBS	WRF	MBE	RMSE	IOA	R
EXP_01	0.242	−0.197	−0.439	2.365	0.951	0.911
EXP_04	13.735	12.577	−1.158	2.629	0.921	0.888
EXP_07	26.239	25.735	−0.504	1.905	0.888	0.806
EXP_10	15.172	14.831	−0.340	2.244	0.947	0.901
W.S. [ms^{-1}]	**OBS**	**WRF**	**MBE**	**RMSE**	**IOA**	**R**
EXP_01	2.265	4.204	1.939	2.778	0.677	0.649
EXP_04	2.362	3.674	1.312	2.124	0.710	0.624
EXP_07	1.764	2.878	1.113	1.721	0.691	0.608
EXP_10	1.773	3.416	1.643	2.350	0.689	0.668

2.2.2. *The finite difference mass balance method*

The BMB method assumes a direct linear relationship between the NO_2 column density and NO_x emissions. Actual meteorological conditions, however, exhibit a non-linear relationship between the NO_2 column density and NO_x emissions because of the transport and diffusion of NO_2 in the atmosphere, which prompts a NO_x-OH chemical reaction (Gu et al., 2016). To compensate for the reaction, the FDMB method reduces the error of the BMB method that occurs in a simple linear process by supplementing the NO_2 column density ($\frac{\Delta\Omega}{\Omega}$) with the change in NO_x emissions ($\frac{\Delta E}{E}$) (Lamsal et al., 2011). The change in NO_x emissions and the simulated changes in the tropospheric NO_2 column density are expressed in Eq. (2) (Walker et al., 2010; Lamsal et al., 2011; Li et al., 2019).

$$\frac{\Delta\Omega}{\Omega}=\beta\frac{\Delta E}{E},\beta=\frac{\Delta\Omega_a/\Omega_a}{\Delta E_a/E_a} \quad \text{(Eq. 2)}$$

where β, a unitless scaling factor that explains the sensitivity of the NO_2 column density for NO_x emissions is calculated from a simulation with Ea and Ea perturbed by 10% (Cooper et al., 2017; Li et al., 2019). β has a value of 0.1–10, to avoid unrealistic emission constraints (Cooper et al., 2017). Based on Eq. (2), an equation for the FDMB method, such as Eq. (3), can be derived. E_t represents NO_x emissions with the top-down approach, E_a the prior NO_x emissions, Ω_o the observed NO_2 column density, and Ω_a the simulated NO_2 column density. Unlike the BMB method, the FDMB method calculates the sensitivity of the NO_2 column density to NO_x emissions. The advantage of the FDMB method is that it quantitatively accounts for the effect of the NO_x emissions of one grid on NO_2 concentrations of the corresponding grid. During the sensitivity (β) calculation process, however, the sensitivities of all NO_x sources in the model domain are mixed because of the advection and diffusion of NO_2, thereby causing errors.

Table 4
Application time and computational cost of the IFDMB method based on modeling resolutions.

	EXP_27 km	EXP_9 km	EXP_3 km
Number of model iterations	8	14	24
Result capacity (Gb/iteration)	4.8	40	354
Modeling time (minutes/iteration)	10	70	456

$$E_t=E_a\left(1+\frac{\Omega_o-\Omega_a}{\beta\Omega_a}\right) \quad \text{(Eq. 3)}$$

2.2.3. *The iterative finite difference mass balance method*

Through the iterative calculation of the model, the IFDMB method reduces errors related to the mixed sensitivities of the FDMB method. A schematic diagram of the IFDMB method appears in Fig. 2. Applying Eqs. 2 and 3, the IFDMB method updates the β term and top-down emissions ($E_t(N)$) via simulation using the top-down emissions ($E_t(N-1)$), calculated by the FDMB method. This process is repeated until the normalized mean difference of the updated emissions ($E_t(N)$) for prior emissions ($E_t(N-1)$) becomes less than 1%. If emissions are updated by iterative modeling, FDMB can reduce the errors caused by its mixed sensitivities by constraining the NO_x emissions until the model-driven NO_2 column density is the closest to the observed NO_2 column density.

2.3. *Pseudo-observation test*

We conducted the pseudo-observation test to suggest conditions for the effective application of mass balance-based inverse modeling methods (i.e., BMB, FDMB, and IFDMB) in South Korea. Even if emis-

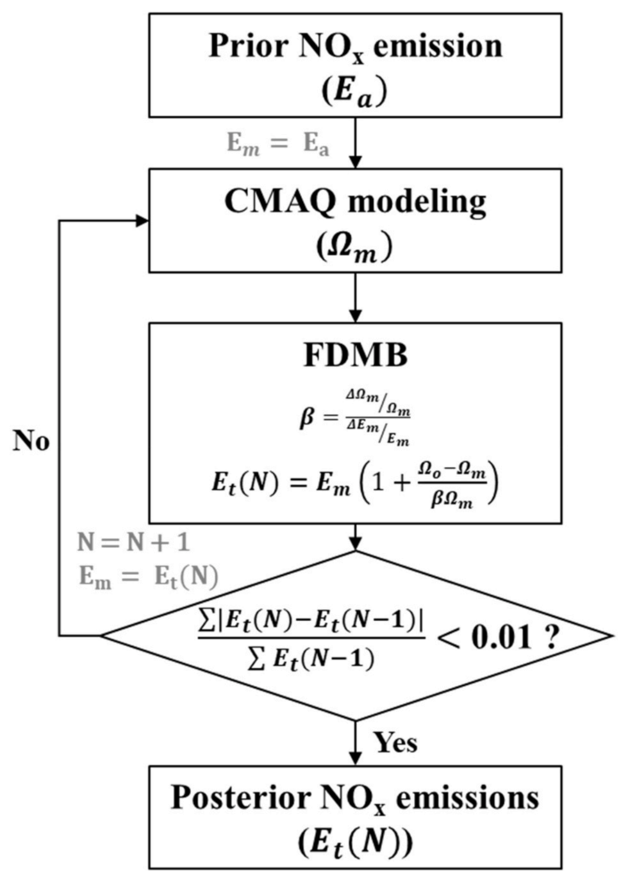

Fig. 2. Flowchart of the iterative finite difference mass balance (IFDMB) method.

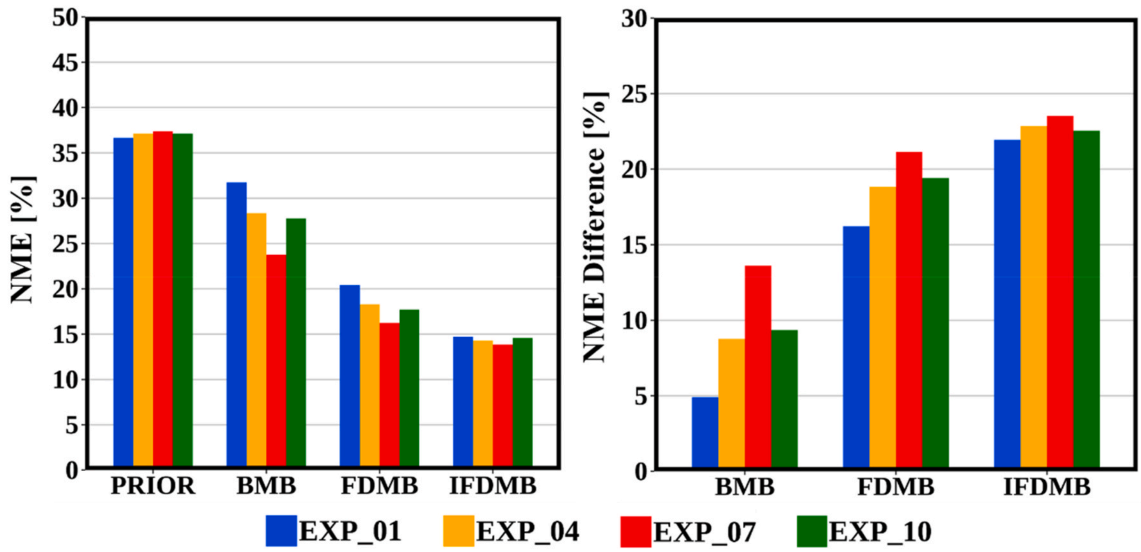

Fig. 3. NME distributions (left) and the difference (right) between the NO_x emissions before and after inverse modeling of each season. BMB: basic mass balance; FDMB: finite difference mass balance; IFDMB: iterative finite difference mass balance; NME: normalized mean error; EXP_01: January; EXP_04: April, EXP_07: July; EXP_10: October.

sions are constrained through inverse modeling based on observational data, actual emissions cannot be identified; hence, it is virtually impossible to verify emissions before and after the constraints. Therefore, we conducted the pseudo-observation test, which was designed to quantitatively verify the accuracy of the inverse modeling method. The pseudo-observation test consists of the following three steps. First, we prepared two different emission inventories and assumed that one was the actual or "true" emissions (E_{true}) and the other was "prior" emissions. Second, we used the model results simulated numerically through the "true" emissions, or the pseudo-observation (POBS) emissions, as observational data in the inverse modeling process. Third, using inverse modeling, we took the results of the numerically simulated model through "prior" emission and POBS data to constrain the emissions. Finally, based on "true" emissions, the effect of applying inverse modeling was quantitatively evaluated via differences between normalized mean error (NME) of the emissions before and after using the inverse modeling (Eq. 4). In this study, we assumed that CAPSS 2016 emissions were "prior" emissions and CAPSS 2017 emissions "true" emissions (Fig. S1) and then applied inverse modeling based on the results of modeling using each emission type.

$$NME = \frac{\sum |E - E_{true}|}{\sum E_{true}} \times 100\ [\%] \quad \text{(Eq. 4)}$$

Air pollutants emitted from sources can be transported to other areas, resulting in high concentrations in the receptor region. Such transport could cause uncertainties in the results from inverse modeling based on mass balance, that is, the smearing effect, a consequence of the spatial difference between the source and the receptor caused by the transport of pollutants. Both the meteorological conditions and model resolution in the inverse modeling situation, which determine the intergrid traveling distance of pollutants, contribute to the smearing effect (Li et al., 2019). Therefore, to reduce the smearing effect before inverse modeling, we averaged the numerically simulated NO_2 column density over the study period (one month). In addition, to identify the effects of the application of inverse modeling in South Korea, we conducted tests based on the seasons and thethe modeling resolutions, both of which influenced the smearing effect. In addition, while using satellite observational data, we conducted the inverse modeling test based on the differences among the regridding methods.

3. Results and discussion results

3.1. *The accuracy of inverse modeling: Seasonal differences*

The effects of inverse modeling may show seasonal differences because wind patterns and the various meteorological factors (e.g., sunlight, temperature, water vapor, and the boundary layer height) that characterize the lifetime of NO_2 and its transportation in the atmosphere vary according to the season (Valin et al., 2013). Therefore, to compare the effect of NO_x emissions by inverse modeling, we performed the pseudo-observation test at a model resolution of 27 km in the winter (January), the spring (April), the summer (July), and the autumn (October) of 2017 in South Korea. We identified the numerical simulation tests for each season with the following labels: EXP_01 (January), EXP_04 (April), EXP_07 (July), and EXP_10 (October).

Prior to analyzing the accuracy of seasonal inverse modeling, we verified the meteorological modeling based on ASOS temperature and wind speed observational data to confirm whether the model simulated the meteorological factors of each season well (Table 3). For verification, we used the following statistical indicators: the mean bias error (MBE), the root mean square error (RMSE), the index of agreement (IOA), and the correlation coefficient (R) (Table S1). As the results of the meteorological simulation satisfied IOAs of $>$0.7 for the temperature and $>$0.6 for the wind speed, in all seasons, the results were statistically significant (Emery et al., 2001). Thus, we confirmed that the model simulated the weather of each season well.

The NME distribution and difference between the NO_x emissions before and after the inverse modeling (BMB, FDMB, and IFDMB) for each season appear in Fig. 3. The figure shows positive NME difference before and after inverse modeling, indicating that the inverse modeling reduced emission errors. The results of the modeling of all four seasons (Fig. 3), from the highest to the lowest accuracy were as follows: IFDMB, FDMB, and BMB methods. The differences between the seasonal results of the BMB and FDMB methods before and after inverse modeling were relatively larger than those of the IFDMB method. Such results can be explained by the smearing effect, which differed depending on the characteristics of the meteorological factors of each season. In the case of the BMB method, which was the most vulnerable to the smearing effect, the inverse modeling accuracy (i.e., the NME difference) in the summer (13.61%) showed a difference of as much as 8.70% compared to the accuracy in the spring (8.77%), the autumn (9.36%), and the winter

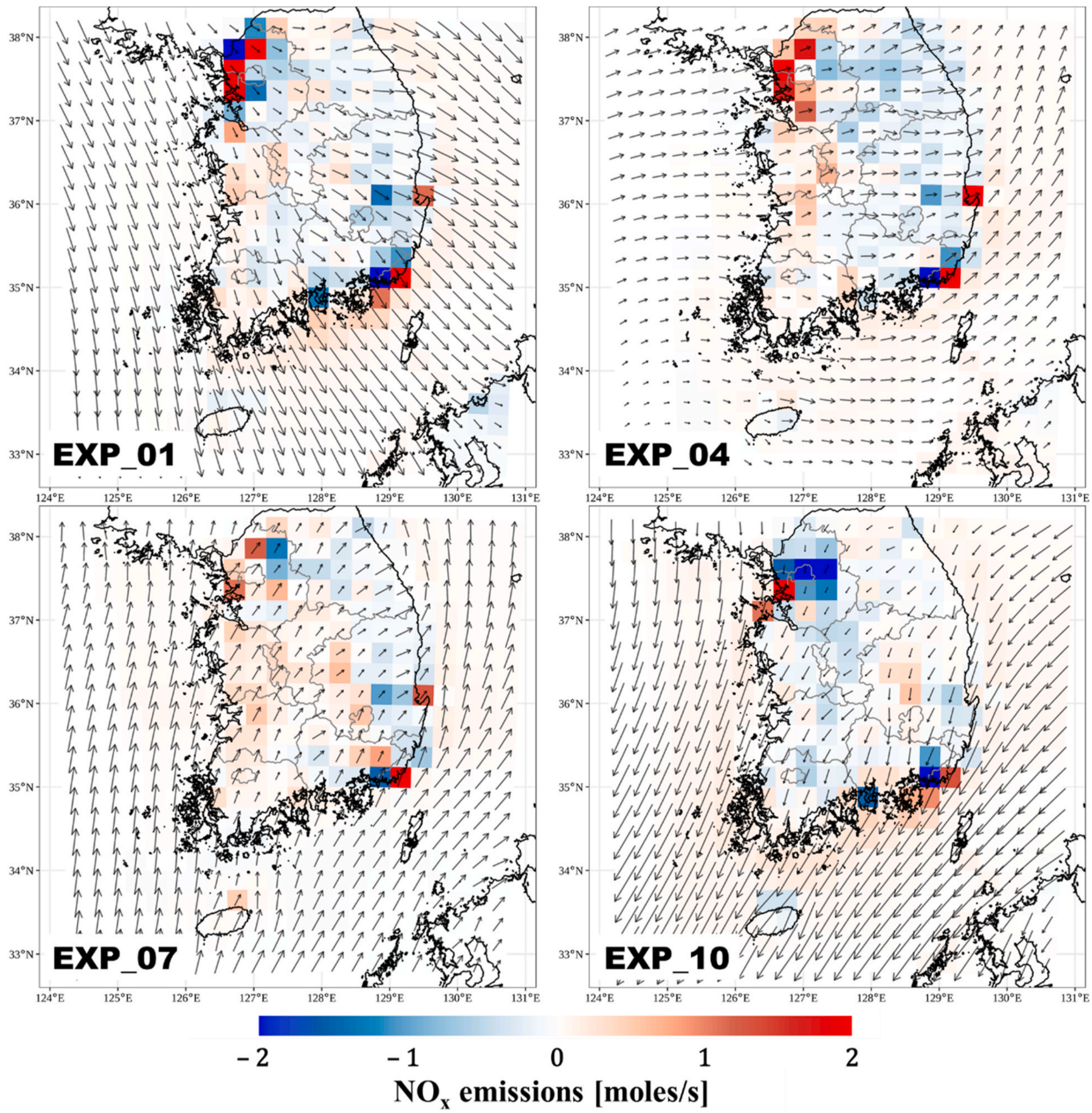

Fig. 4. Difference between the constrained NO_x emissions found by the iterative finite difference mass balance (IFDMB) method by each season and the "true" NO_x emissions. EXP_01: January; EXP_04: April, EXP_07: July; EXP_10: October.

(4.91%). Conversely, lacking the vulnerability of the BMB and FDMB methods, the IFDMB method showed similar accuracy in all seasons (only as much as a 1.58% difference). Here, it should be noted that the mass balance-based inverse modeling methods used in this study (BMB, FDMB, and IFDMB) cannot explicitly take into account the transport of pollutants inducing the smearing effect. However, the IFDMB method showed better results than the BMB and FDMB methods because it reduced the errors through iterative calculations, minimizing the smearing effect. Thus, the effects of the IFDMB method in the application of inverse modeling were the best for all seasons.

Upon review of the seasonal differences in the accuracy of inverse modeling, we noted the highest accuracy in the summer (EXP_07) and the lowest in the winter (EXP_01) in all experiments. Higher temperatures in the summer shorten the lifetime of NO_2 in the atmosphere (Goldberg et al., 2021), and lower the wind speed. Therefore, our study showed that the smearing effect resulted in the least number of emissions errors in the summer, so the application of inverse modeling showed the highest accuracy. By contrast, the lower temperatures in the winter lengthen the lifetime of NO_2 (Shah et al., 2020) and increase the wind speed. Thus, our study showed that the smearing effect, caused by the transport of NO_2, was the greatest in the winter, so the application of inverse modeling resulted in the lowest accuracy.

We also examined the spatial distribution of the accuracy of the inverse modeling of NO_x emissions based on seasons. As the IFDMB method was the most accurate for all seasons, we used this method to analyze seasonal NO_x emissions in South Korea (Fig. S2) and found high NO_x emissions near the downtown areas of Seoul and Busan, both home to a large number of NO_x emission sources. In particular, Seoul showed >50 mol/s of NO_x emissions, which was significantly higher than in other areas. Applying the IFDMB method for each season, we evaluated the spatial distribution of the accuracy of inverse modeling by examining the difference between constrained emissions and "true" emissions

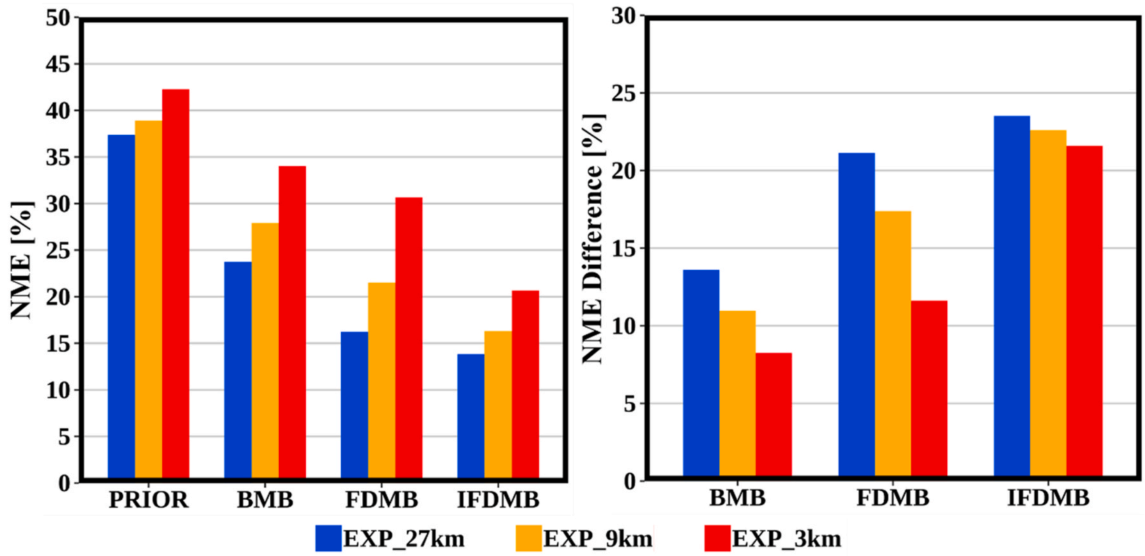

Fig. 5. Normalized mean error (NME) distribution (left) and the difference (right) between the NO_x emissions before and after inverse modeling according to the model resolution. EXP_27 km, EXP_9 km, and EXP_3 km represent modeling resolutions for the South Korea at 27, 9, and 3 km, respectively. BMB: basic mass balance; FDMB: finite difference mass balance; IFDMB: iterative finite difference mass balance.

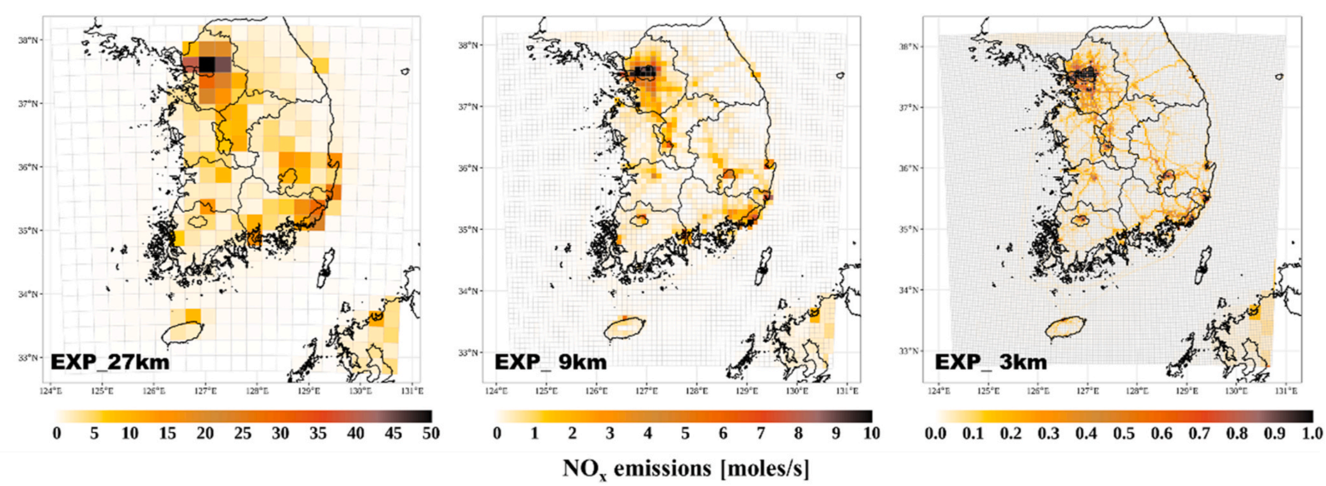

Fig. 6. Distribution of "true" NO_x emissions according to the model resolution. EXP_27 km, EXP_9 km, and EXP_3 km represent the modeling resolutions for the South Korean region at 27, 9, and 3 km, respectively.

(Fig. 4). After inverse modeling for all seasons, we found emission errors mainly in the urban areas of Seoul and Busan, where NO_x emissions were high. Furthermore, the spatial difference between NO_x emissions before and after inverse modeling varied by season. This finding can be explained by the variation in the direction of NO_2 transport, which depends on the seasonal wind field; hence, the spatial distribution of the smearing effect varied in the inverse modeling process. One noteworthy thing is that emission errors were also found in coastal areas (especially the southern coastal area). These errors were analyzed to be attributable to the smearing effect caused by the transport of NO_2 because they mainly appeared on the downwind side of emission sources, and rarely appeared in summer. Since the sea has a relatively small distribution of anthropogenic emissions compared to the inland, the emission changes in the coastal areas may be somewhat unrealistic. Therefore, these results need to be sufficiently verified through the use of remote sensing data in future follow-up studies.

The above results suggest that the accuracy of NO_x inversion in South Korea varies according to seasonal meteorological factors. Therefore, to maximize the accuracy of inverse modeling, we suggest selecting a period in the summer when the smearing effect is less than it is in other seasons.

3.2. *The accuracy of inverse modeling: Differences in model resolutions*

Previous studies have applied inverse modeling to model domains with coarse resolutions (Cooper et al., 2017; Qu et al., 2017, 2019; Chen et al., 2021). As the accurate simulation of the air quality of South Korea, which has a complex topography, requires high-resolution modeling (Bae et al., 2020; Jeong et al., 2020), the accuracy of inverse modeling on fine (i.e., high-resolution) grids should be verified. Thus, we examined the difference between the accuracy of the inverse modeling of various resolutions for the summer, with fewer emission errors. The modeling resolutions were set at 27, 9, and 3 km, and we labeled the corresponding tests for each resolution EXP_27 km, EXP_9 km, and EXP_3 km, respectively. The number of grids applied to each resolution is shown in Table 1.

The NME distribution and the difference between the NO_x emissions before and after inverse modeling according to the modeling resolution appear in Fig. 5. NME values of the "prior" emissions were larger at the finer resolutions, which led to a denser spatial distribution of the grid corresponding to the emission source in the same area and thereby increased the difference between the "prior" and "true" emissions (Fig. 6). The accuracy of inverse modeling, from the most to the least accurate, was of the IFDMB, FDMB, and BMB methods at all resolutions, indicating that the IFDMB method was the most effective even at a higher modeling resolution. It is worth noting that the differences in the accuracy of the inverse modeling by the IFDMB method at the modeling resolutions (i.e., EXP_27 km, EXP_9 km, and EXP_3 km) were relatively smaller than those of the other two methods (FDMB and BMB). After all, the iterative modeling of the IFDMB method minimized differences among the smearing effects at the various modeling resolutions (i.e., the higher the resolution, the larger the smearing effect). Hence, the IFDMB method appears to be the most effective for high-resolution inverse modeling.

The effect of high-resolution inverse modeling in the IFDMB method is similar to that of low-resolution modeling, it, however, involves a significant amount of time and high computational cost. For example, the number of model iterations of EXP_3 km was approximately three times as high as those of EXP_27 km, the output capacity was approximately 74 times as high, and the computational time (28 CPUs of Intel (R) Xeon(R) E5-2697A v4.2.6 Ghz) was approximately 46 times as high (Table 4). Therefore, the computational resources required to apply the IFDMB method increase significantly as the modeling resolution increases. As the accuracy of inverse modeling, however, does not significantly improve, it is important to set an appropriate resolution of the modeling. Modeling resolutions 27 km and 3 km were limited in their capability of indicating the effect of local emissions and high computational costs, respectively. Furthermore, the spatial resolutions of representative satellite observational data available for inverse modeling in South Korea are 13 × 24 km (OMI), 7.5 × 3.5 km (TROPOMI), and 7 × 8 km (GEMS). As the resolutions of the satellite data are generally coarser than 3 km, the 3 km modeling resolution may not be as effective for inverse modeling as other resolutions. Therefore, a modeling resolution of approximately 9 km might be considered the most appropriate for inverse modeling using the IFDMB method in South Korea. After all, the accuracy of inverse modeling at a 9 km resolution does not differ significantly from the accuracy at 27 km; in addition, modeling at a 9 km resolution is more cost-effective than that at 3 km, and the grid size is similar to that of available satellite observation data.

3.3. The accuracy of inverse modeling: Differences among regridding methodologies

The mass balance-based inverse modeling methodology determines top-down NO_x emissions by the difference between the NO_2 column density distributions of observations and model results. Since satellite pixels and model grids are inconsistent, the process of regridding observed data into the model grid should be performed first. The spatial distribution of gridded observational data, however, may differ depending on the regridding method. As mass balance-based inverse modeling uses the final gridded model and observational data, spatial differences during the regridding process may cause severe errors in inverse modeling. Therefore, we compared the accuracy of inverse modeling according to the regridding method.

The period for the test modeling was July 2017, the selected inverse modeling resolution was 9 km (based on Section 3.2), the most efficient, and the size of the observation pixel was set to an OMI footprint pixel of 13 × 24 km. To compare the accuracy of inverse modeling based on the regridding method, we used POBS data in the same manner as we did in Sections 3.1 and 3.2. We generated pseudo-OMI data by upscaling POBS data corresponding to pixels passing through South Korea (domain D2) among OMI NO_2 column density data during the study period. We regridded the pseudo-OMI data to fit the model grid based on conservative regridding and downscaling methods suggested by Kim et al. (2018) and converted them to the form applicable for inverse modeling. The conservative regridding process follows: After calculating the overlapping ratio ($f_{i,j}$) of the pseudo-OMI pixel (P_i) area to the CMAQ grid (C_j), we allocate the pseudo-OMI data to the CMAQ grid (Fig. 7a). The conservative downscaling method then applies downscaling to the conservative regridding method. Through the CMAQ grid data within the pseudo-OMI pixels, the spatial weighting kernel ($k_{i,j}$) is calculated and indicates the detailed spatial distribution of the NO_2 column density within the pseudo-OMI pixels (Fig. 7b and c). We refer to the conservative regridding and downscaling methods as the xDS and DS methods, respectively, and the corresponding equations are Eqs. (5) and (6). In addition, we extract POBS data of NO_2 column density, which corresponds to OMI footprint-pixel. In theory, extracted data are already gridded and regarded as ideal data in which pseudo-OMI data are accurately regridded. Therefore, as this method can exclude errors that occur during the process of spatially regridding pseudo-OMI data to the CMAQ grid, we expect it to perform the application of inverse modeling ideally. This regridding method, which we refer to as the GRID method, is a control test for the quantitative comparison of the effects of errors occurring in the regridding process of the xDS and DS methods on inverse modeling. Finally, we applied inverse modeling based on POBS data regridded using the three methods and compared their accuracy based on the regridding method.

$$C_j = \frac{\sum P_i \bullet f_{i,j}}{\sum f_{i,j}}, \text{ where } f_{i,j} = \frac{Area(P_i \cap C_j)}{Area(C_j)} \qquad \text{(Eq. 5)}$$

$$C_j = \frac{\sum P_i \bullet k_{i,j} \bullet f_{i,j}}{\sum f_{i,j}}, \text{where } k_{i,j} \text{ is the spatial weighting kernel of } P_i \text{ in the position of } C_j \qquad \text{(Eq. 6)}$$

Fig. 8 illustrates the distribution of pseudo-OMI data according to the regridding method. The DS method, unlike the xDS method, indicates the detailed spatial distribution of the pseudo-OMI NO_2 column density. In addition, while the xDS method shows that NO_2 column density is equally allocated to the model grid within the OMI pixels, the DS method shows that the CMAQ grid overlapping the OMI pixel is differentially allocated by using the spatial weighting kernel. As a result, the distribution of the NO_2 column density via the DS method shows strong spatial agreement with that via the GRID method, while the xDS method does not.

We applied inverse modeling based on the NO_2 column density allocated to the model grid according to the regridding method and labeled the inverse modeling tests based on the three regridding methods: EXP_xDS, EXP_DS, and EXP_GRID. While the application of the inverse modeling tests EXP_GRID and EXP_DS reduced the NME of emissions, that of EXP-xDS increased the NME (Fig. 9). As shown in Fig. 8, since the distribution of the POBS NO_2 column density calculated by the xDS method did not accurately show the distribution of NO_x emission sources, the NME of emissions were assumed to increase after the application. Meanwhile, the NME of emissions found by EXP_DS was higher than that found by EXP_GRID. An explanation of this difference is that it originates from errors resulting from spatial differences among the DS methods among the actual distributions during the calculation process of the spatial weighting kernel that determines the spatial fraction of NO_x emissions within the OMI pixels.

As a result, the use of satellite observational data for inverse modeling necessitates a regridding process according to a modeling resolution; errors, however, may occur during the process. Therefore, we recommended using satellite data with a resolution similar to that of the model grid to the extent possible and applying a method that minimizes errors in the regridding process. The DS method used in this study, in which the spatial distribution of emissions is well represented with relatively fewer errors during the regridding process, is more effective than the xDS method. If the DS method is not applied, and instead, satellite observation data with a lower spatial resolution than

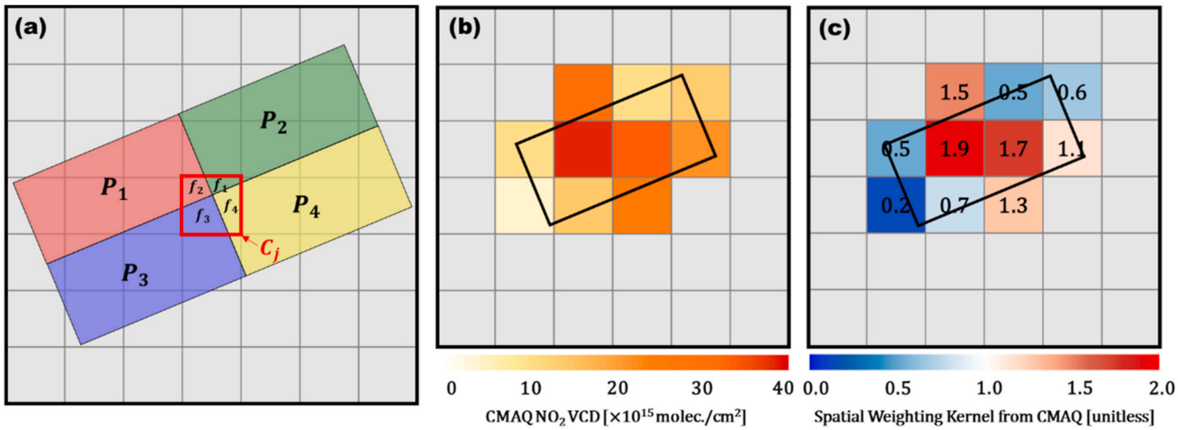

Fig. 7. Example of the conservative regridding and conservative downscaling methods. (a) Schematic diagram of the conservative regridding method. (b) Distribution of the community multi-scale air quality model (CMAQ) NO_2 vertical column density. (c)Distribution of the spatial weighting kernel from CMAQ.

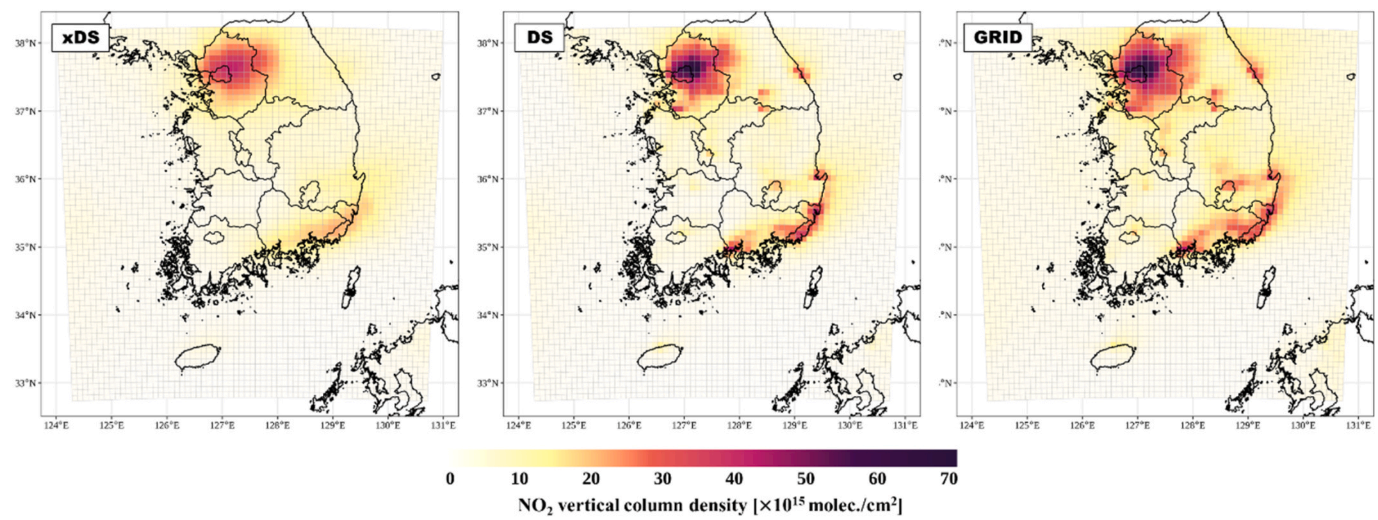

Fig. 8. Pseudo-ozone monitoring instrument (pseudo-OMI) NO_2 vertical column density distribution according to the regridding method. xDS: conservative regridding method; DS: conservative downscaling method; GRID: the most precise, ideal regridding pseudo-OMI data method.

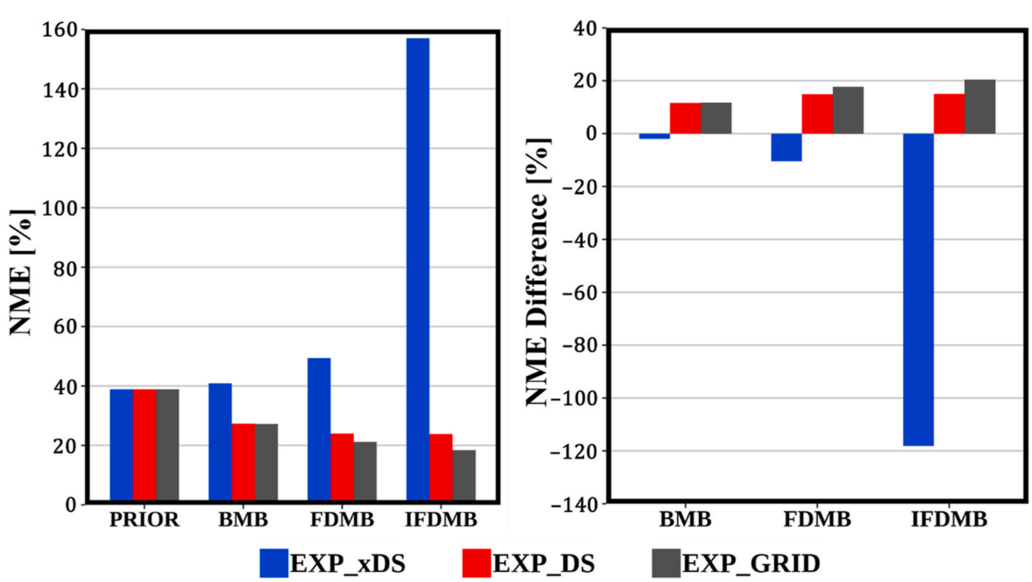

Fig. 9. Normalized mean error (NME) distributions (left) and differences (right) among the methods before and after inverse modeling according to the regridding method. BMB: basic mass balance; FDMB: finite difference mass balance; IFDMB: iterative finite difference mass balance.

that of the model are used as is, the emission distribution characteristics cannot be accurately expressed after the application of inverse modeling, leading to more errors resulting from the spatial difference in emissions. Therefore, when the spatial resolutions of observations and the model differ, one must apply the regridding method so that the spatial distribution characteristics of emissions are well represented while considering the resolutions of the two types of data.

4. Summary and conclusion

We constrained NO_x emissions based on the mass balance-based inverse modeling methods, BMB, FDMB, and IFDMB, in South Korea. To quantitatively compare the accuracy of inverse modeling, we used the CMAQ model and conducted pseudo-observation tests. We evaluated the ability of inverse modeling by comparing NO_x emission errors before and after inverse modeling and the accuracy of the inverse modeling of the methods according to the season, the modeling resolution, and the regridding methods that suggest inverse modeling conditions suitable for South Korea.

We analyzed the results of the aforementioned three methods. First, we found that the seasonal inverse modeling accuracy was highest in the summer, the most optimal season for performing inverse modeling of NO_x emissions in South Korea. High temperatures in the summer enhance the chemical reaction of NO_2, and shorten the lifetime of NO_2 with the reduced wind speed, thus decreasing the smearing effect caused by transport and diffusion. In addition, we found that the lower the resolution was, the greater the accuracy of the inverse modeling. With regard to the modeling resolution, however, the results of the IFDMB method did not significantly differ from those of the BMB and FDMB methods, which we attribute to iterative calculation, which minimizes errors.

Finally, we investigated the effect of the application of inverse modeling based on the gridding method using pseudo-OMI data. As a result, depending on the application of downscaling, the spatial distribution of NO_x emissions significantly changed after the application of inverse modeling. After applying inverse modeling using the DS method with the downscaling application, we found fewer emission errors; in the case of the xDS method without the downscaling application, however, the number of emission errors increased. Therefore, the use of satellite observational data for inverse modeling based on mass balance necessitates regridding according to the modeling resolution and application methods that clearly represent the spatial distribution characteristics of emissions by considering the resolutions of the two types of data.

Overall, the IFDMB method was the most effective at constraining NO_x emissions through mass balance-based inverse modeling for South Korea. This method achieves optimal efficiency while modeling at a resolution of 9 km during the summer. In addition, when using satellite data with a large difference in resolution from that of the model, one needs to apply a regridding method using downscaling to more accurately represent the spatial distribution of emissions.

This study quantitatively evaluated the accuracy of inverse modeling using pseudo-observational data instead of actual observational data. These results are expected to contribute to the advancement of studies related to inverse modeling that use actual satellite observational data such as OMI, TROPOMI, and GEMS.

CRediT authorship contribution statement

Jeonghyeok Mun: Conceptualization, Formal analysis, Writing – original draft. **Yunsoo Choi:** Writing – review & editing, Supervision. **Wonbae Jeon:** Conceptualization, Writing – review & editing, Supervision. **Hwa Woon Lee:** Supervision. **Cheol-Hee Kim:** Project administration, Funding acquisition. **Soon-Young Park:** Validation. **Juseon Bak:** Writing – review & editing. **Jia Jung:** Writing – review & editing. **Inbo Oh:** Formal analysis. **Jaehyeong Park:** Formal analysis, Investigation. **Dongjin Kim:** Validation, Resources.

Declaration of competing interest

The authors declare that they have no known competing financial interests or personal relationships that could have appeared to influence the work reported in this paper.

Data availability

Data will be made available on request.

Acknowledgments

This research was supported by the Basic Science Research Program through the National Research Foundation of Korea (NRF) funded by the Ministry of Education (NRF-2020R1A6A1A03044834). J. Jung is supported by NASA grant #80HQTR21T0069at Pacific Northwest National Laboratory (PNNL). PNNL is operated for DOE by Battelle Memorial Institute under contract DE-AC06-76RLO 1830.

Appendix B. Supplementary data

Supplementary data to this article can be found online at https://doi.org/10.1016/j.atmosenv.2022.119429.

Appendix A. Supporting information

Supplementary data associated with this article can be found in the online version at doi:

References

Appel, K.W., Bash, J.O., Fahey, K.M., Foley, K.M., Gilliam, R.C., Hogrefe, C., Hutzell, W. T., Kang, D., Mathur, R., Murphy, B.N., Napelenok, S.L., Nolte, C.G., Pleim, J.E., Pouliot, G.A., Pye, H.O.T., Ran, L., Roselle, S.J., Sarwar, G., Schwede, D.B., Sidi, F.I., Spero, T.L., Wong, D.C., 2021. The Community Multiscale Air Quality (CMAQ) model versions 5.3 and 5.3.1: system updates and evaluation. Geosci. Model Dev. (GMD) 14, 2867–2897. https://doi.org/10.5194/gmd-14-2867-2021.

Bae, C., Kim, B.-U., Kim, H.C., Kim, S., 2018. Quantitative assessment on contributions of foreign NO_x and VOC emission to ozone concentrations over gwangyang bay with CMAQ-HDDM simulations. J. Korean Soc. Atmos. Environ. 34 (5), 708–726. https://doi.org/10.5572/kosae.2018.34.5.708.

Bae, M., Kim, B.U., Kim, H.C., Kim, S., 2020. A multiscale tiered approach to quantify contributions: a case study of $PM_{2.5}$ in South Korea during 2010-2017. Atmosphere 11 (2), 5–15. https://doi.org/10.3390/atmos11020141.

Cheng, X., Hao, Z., Zang, Z., Liu, Z., Xu, X., Wang, S., Liu, Y., Hu, Y., Ma, X., 2021. A new inverse modeling approach for emission sources based on the DDM-3D and 3DVAR techniques: an application to air quality forecasts in the Beijing-Tianjin-Hebei region. Atmos. Chem. Phys. 21 (18), 13747–13761. https://doi.org/10.5194/acp-21-13747-2021.

Chen, Y., Shen, H., Kaiser, J., Hu, Y., Capps, S.L., Zhao, S., Hakami, A., Shih, J.-S., Pavur, G.K., Turner, M.D., Henze, D.K., Resler, J., Nenes, A., Napelenok, S.L., Bash, J.O., Fahey, K.M., Carmichael, G.R., Chai, T., Clarisse, L., Coheur, P.-F., Van Damme, M., Russell, A.G., 2021. High-resolution hybrid inversion of IASI ammonia columns to constrain US ammonia emissions using the CMAQ adjoint model. Atmos. Chem. Phys. 21, 2067–2082. https://doi.org/10.5194/acp-21-2067-2021.

Cooper, M., Martin, R.V., Padmanabhan, A., Henze, D.K., 2017. Comparing mass balance and adjoint methods for inverse modeling of nitrogen dioxide columns for global nitrogen oxide emissions. J. Geophys. Res. Atmos. 122, 4718–4734. https://doi.org/10.1002/2016JD025985.

Crutzen, P.J., 1979. The role of NO and NO_2 in the chemistry of the troposphere and stratosphere. Annu. Rev. Earth Planet Sci. 7 (1), 443–472. https://doi.org/10.1146/annurev.ea.07.050179.002303.

Emery, C., Tai, E., Yarwood, G., 2001. Enhanced Meteorological Modeling and Performance Evaluation for Two Texas Episodes. Prepared for the Texas Natural Resources Conservation Commission. ENVIRON International Corporation, Novato, CA.

Gilliland, A., Abbitt, P.J., 2001. A sensitivity study of the discrete Kalman filter (DKF) to initial condition discrepancies. J. Geophys. Res. Atmos. 106, 17939–17952. https://doi.org/10.1029/2001JD900174.

Goldberg, D.L., Anenberg, S.C., Kerr, G.H., Mohegh, A., Lu, Z., Streets, D.G., 2021. TROPOMI NO2 in the United States: a detailed look at the annual averages, weekly cycles, effects of temperature, and correlation with surface NO2 concentrations. Earth's Future 9 (4), 1–16. https://doi.org/10.1029/2020EF001665.

Gu, D., Wang, Y., Yin, R., Zhang, Y., Smeltzer, C., 2016. Inverse modelling of NO_x emissions over eastern China: uncertainties due to chemical non-linearity. Atmos. Meas. Tech. 9 (10), 5193–5201. https://doi.org/10.5194/amt-9-5193-2016.

Han, K.M., Lee, S., Chang, L.S., Song, C.H., 2015. A comparison study between CMAQ-simulated and OMI-retrieved NO_2 columns over East Asia for evaluation of NO_x emission fluxes of INTEX-B, CAPSS, and REAS inventories. Atmos. Chem. Phys. 15 (4), 1913–1938. https://doi.org/10.5194/acp-15-1913-2015.

Hu, J., Chen, J., Ying, Q., Zhang, H., 2016. One-year simulation of ozone and particulate matter in China using WRF/CMAQ modeling system. Atmos. Chem. Phys. 16 (16), 10333–10350. https://doi.org/10.5194/acp-16-10333-2016.

Itahashi, S., Uno, I., Kim, S., 2013. Seasonal source contributions of tropospheric ozone over East Asia based on CMAQ-HDDM. Atmos. Environ. 70, 204–217. https://doi.org/10.1016/j.atmosenv.2013.01.026.

Jeong, J.H., Oh, I., Kang, Y.H., Bang, J.H., An, H., Seok, H.B., Kim, Y.K., Hong, J., Kim, J., 2016. WRF modeling approach for improvement of air quality modeling in the Seoul metropolitan region: seasonal sensitivity analysis of the WRF physics options. J. Environ. Sci. 25 (1), 67–83. https://doi.org/10.5322/jesi.2016.25.1.67.

Jeong, Y., Lee, H.W., Jeon, W., 2020. Regional differences of primary meteorological factors impacting O3 variability in South Korea. Atmosphere 11 (1). https://doi.org/10.3390/ATMOS11010074.

Jeon, W., Choi, Y., Lee, H.W., Lee, S.H., Yoo, J.W., Park, J., Lee, H.J., 2015. A quantitative analysis of grid nudging effect on each process of $PM_{2.5}$ production in the Korean Peninsula. Atmos. Environ. 122, 763–774. https://doi.org/10.1016/j.atmosenv.2015.10.050.

Jung, J., Choi, Y., Souri, A.H., Mousavinezhad, S., Sayeed, A., Lee, K., 2022. The impact of springtime-transported air pollutants on local air quality with satellite-constrained NOx emission adjustments over East Asia. J. Geophys. Res. Atmos. 127 (5), 1–18. https://doi.org/10.1029/2021jd035251.

Kim, H.C., Lee, S.M., Chai, T., Ngan, F., Pan, L., Lee, P., 2018. A conservative downscaling of satellite-detected chemical compositions: NO_2 column densities of OMI, GOME-2, and CMAQ. Rem. Sens. 10, 1001. https://doi.org/10.3390/rs10071001.

Kim, J., Ghim, Y.S., Han, J.-S., Park, S.-M., Shin, H.-J., Lee, S.-B., Kim, J., Lee, G., 2018. Long-term trend analysis of Korean air quality and its implication to current air quality policy on ozone and PM_{10}. J. Korean Soc. Atmos. Environ. 34 (1), 1–15. https://doi.org/10.5572/kosae.2018.34.1.001.

Kitayama, K., Morino, Y., Yamaji, K., Chatani, S., 2019. Uncertainties in O_3 concentrations simulated by CMAQ over Japan using four chemical mechanisms. Atmos. Environ. 198, 448–462. https://doi.org/10.1016/j.atmosenv.2018.11.003.

Kurokawa, J. ichi, Yumimoto, K., Uno, I., Ohara, T., 2009. Adjoint inverse modeling of NO_x emissions over eastern China using satellite observations of NO_2 vertical column densities. Atmos. Environ. 43 (11), 1878–1887. https://doi.org/10.1016/j.atmosenv.2008.12.030.

Lamsal, L.N., Martin, R.v., Padmanabhan, A., van Donkelaar, A., Zhang, Q., Sioris, C.E., Chance, K., Kurosu, T.P., Newchurch, M.J., 2011. Application of satellite observations for timely updates to global anthropogenic NO_x emission inventories. Geophys. Res. Lett. 38 (5), 1–5. https://doi.org/10.1029/2010GL046476.

Lawrence, M.G., Crutzen, P.J., 1999. Influence of NO_x emissions from ships on tropospheric photochemistry and climate. Nature 402, 167–170. https://doi.org/10.1038/46013.

Lee, G., Park, J.H., Kim, D.G., Koh, M.S., Lee, M., Han, J.S., Kim, J.C., 2020. Current status and future directions of tropospheric photochemical ozone studies in Korea. J. Korean Soc. Atmos. Environ. 36 (4), 419–441. https://doi.org/10.5572/KOSAE.2020.36.4.419.

Lee, H.W., Cha, Y.M., Lee, S.H., Kim, D.H., 2010. Impact of high-resolution sea surface temperatures on the simulated wind resources in the southeastern coast of the Korean Peninsula. J. Environ. Sci. Int. 19, 171–184.

Leue, C., Wenig, M., Wagner, T., Klimm, O., Platt, U., Jahne, B., 2001. Quantitative analysis of NO_2 emissions from Global Ozone Monitoring Experiment satellite image sequences. J. Geophys. Res. 106, 5493–5505. https://doi.org/10.1029/2000JD900572.

Li, C., Martin, R.V., Shephard, M.W., Cady-Pereira, K., Cooper, M.J., Kaiser, J., Lee, C.J., Zhang, L., Henze, D.K., 2019. Assessing the iterative finite difference mass balance and 4D-Var methods to derive ammonia emissions over North America using synthetic observations. J. Geophys. Res. Atmos. 124, 4222–4236. https://doi.org/10.1029/2018JD030183.

Li, M., Zhang, Q., Kurokawa, J.I., Woo, J.H., He, K., Lu, Z., Ohara, T., Song, Y., Streets, D. G., Carmichael, G.R., Cheng, Y., Hong, C., Huo, H., Jiang, X., Kang, S., Liu, F., Su, H., Zheng, B., 2017. MIX: a mosaic Asian anthropogenic emission inventory under the international collaboration framework of the MICS-Asia and HTAP. Atmos. Chem. Phys. 17, 935–963. https://doi.org/10.5194/acp-17-935-2017.

Lin, J.T., Liu, Z., Zhang, Q., Liu, H., Mao, J., Zhuang, G., 2012. Modeling uncertainties for tropospheric nitrogen dioxide columns affecting satellite-based inverse modeling of nitrogen oxides emissions. Atmos. Chem. Phys. 12 (24), 12255–12275. https://doi.org/10.5194/acp-12-12255-2012.

Liu, S., Jiang, X., Tsona, N.T., Lv, C., Du, L., 2019. Effects of NO_x, SO_2 and RH on the SOA formation from cyclohexene photooxidation. Chemosphere 216, 794–804. https://doi.org/10.1016/j.chemosphere.2018.10.180.

Martin, R.v., Jacob, D.J., Chance, K., Kurosu, T.P., Palmer, P.I., Evans, M.J., 2003. Global inventory of nitrogen oxide emissions constrained by space-based observations of NO_2 columns. J. Geophys. Res. Atmos. 108 (17), 1–12. https://doi.org/10.1029/2003jd003453.

Mun, J., Lee, H.W., Jeon, W., Lee, S.H., 2017. Impact of meteorological initial input data on WRF simulation - comparison of ERA-Interim and FNL data. J. Environ. Sci. 26 (12), 1307–1319.

National Institute of Environmental Research (NIER), 2019. National Air Pollutant Emissions, 2016. http://airemiss.nier.go.kr/user/boardList.do?command=view&page=1&boardId=74&boardSeq=526&id=airemiss_040100000000.

Napelenok, S.L., Pinder, R.W., Gilliland, A.B., Martin, R.v., 2008. A method for evaluating spatially-resolved NO_x emissions using Kalman filter inversion, direct sensitivities, and space-based NO_2 observations. Atmos. Chem. Phys. 8 (18), 5603–5614. https://doi.org/10.5194/acp-8-5603-2008.

Pamler, P.I., Jacob, D.J., Fiore, A.M., Martin, R.v., Chance, K., Kurosu, T.P., 2003. Mapping isoprene emissions over North America using formaldehyde column observations from space. J. Geophys. Res. Atmos. 108 (6) https://doi.org/10.1029/2002jd002153.

Qu, Z., Henze, D.K., Capps, S.L., Wang, Y., Xu, X., Wang, J., Keller, M., 2017. Monthly top-down NOx emissions for China (2005-2012): a hybrid inversion method and trend analysis. J. Geophys. Res. 122 (8), 4600–4625. https://doi.org/10.1002/2016JD025852.

Qu, Z., Henze, D.K., Li, C., Theys, N., Wang, Y., Wang, J., Wang, W., Han, J., Shim, C., Dickerson, R.R., Ren, X., 2019a. SO2 emission estimates using OMI SO2 retrievals for 2005–2017. J. Geophys. Res. Atmos. 124 (14), 8336–8359. https://doi.org/10.1029/2019JD030243.

Qu, Z., Henze, D.K., Theys, N., Wang, J., Wang, W., 2019b. Hybrid mass balance/4D-var joint inversion of NO_x and SO_2 emissions in East Asia. J. Geophys. Res. Atmos. 124 (14), 8203–8224. https://doi.org/10.1029/2018JD030240.

Sarrafzadeh, M., Wildt, J., Pullinen, I., Springer, M., Kleist, E., Tillmann, R., Schmitt, S. H., Wu, C., Mentel, T.F., Zhao, D., Hastie, D.R., Kiendler-Scharr, A., 2016. Impact of NOx and OH on secondary organic aerosol formation from β-pinene photooxidation. Atmos. Chem. Phys. 16 (17), 11237–11248. https://doi.org/10.5194/acp-16-11237-2016.

J. Shah, V., Jacob, D., Li, K., Silvern, R., Zhai, S., Liu, M., Lin, J., Zhang, Q., 2020. Effect of changing NO_x lifetime on the seasonality and long-term trends of satellite-observed tropospheric NO_2 columns over China Atmos. Chem. Phys. 20 (3), 1483–1495. https://doi.org/10.5194/acp-20-1483-2020.

Skamarock, W.C., Klemp, J.B., Dudhia, J., Gill, D.O., Zhiquan, L., Berner, J., Wang, W., Powers, J.G., Duda, M.G., Barker, D.M., Huang, X.-Y., 2019. A Description of the Advanced Research WRF Model Version 4. NCAR Technical Note NCAR/TN-556+STR. 145. http://library.ucar.edu/research/publish-technote.

Souri, A.H., Chance, K., Bak, J., Nowlan, C., González Abad, G., Jung, Y., Wong, D., Mao, J., Liu, X., 2021. Unraveling pathways of elevated ozone induced by the 2020 lockdown in Europe by an observationally constrained regional model: non-linear joint inversion of NO_x and VOC emissions using TROPOMI. Atmos. Chem. Phys. 21, 18227–18245. https://doi.org/10.5194/acp-21-18227-2021.

Souri, A.H., Choi, Y., Jeon, W., Li, X., Pan, S., Diao, L., Westenbarger, D.A., 2016. Constraining NO_x emissions using satellite NO_2 measurements during 2013 DISCOVER-AQ Texas campaign. Atmos. Environ. 131 (2), 371–381. https://doi.org/10.1016/j.atmosenv.2016.02.020.

Souri, A.H., Nowlan, C.R., González Abad, G., Zhu, L., Blake, D.R., Fried, A., Weinheimer, A.J., Wisthaler, A., Woo, J.-H., Zhang, Q., Chan Miller, C.E., Liu, X., Chance, K., 2020. An inversion of NO_x and non-methane volatile organic compound (NMVOC) emissions using satellite observations during the KORUS-AQ campaign and implications for surface ozone over East Asia. Atmos. Chem. Phys. 20 (16), 9837–9854. https://doi.org/10.5194/acp-20-9837-2020.

Streets, D.G., Bond, T.C., Carmichael, G.R., Fernandes, S.D., Fu, Q., He, D., Klimont, Z., Nelson, S.M., Tsai, N.Y., Wang, M.Q., Woo, J.H., Yarber, K.F., 2003. An inventory of gaseous and primary aerosol emissions in Asia in the year 2000. J. Geophys. Res. 108, 8809. https://doi.org/10.1029/2002jd003093.

Tang, W., Cohan, D.S., Lamsal, L.N., Xiao, X., Zhou, W., 2013. Inverse modeling of Texas NO_x emissions using space-based and ground-based NO_2 observations. Atmos. Chem. Phys. 13 (21), 11005–11018. https://doi.org/10.5194/acp-13-11005-2013.

Valin, L.C., Russell, A.R., Cohen, R.C., 2013. Variations of OH radical in an urban plume inferred from NO_2 column measurements. Geophys. Res. Lett. 40 (9), 1856–1860. https://doi.org/10.1002/grl.50267.

Walker, T.W., Martin, R.v., van Donkelaar, A., Leaitch, W.R., MacDonald, A.M., Anlauf, K.G., Cohen, R.C., Bertram, T.H., Huey, L.G., Avery, M.A., Weinheimer, A.J., Flocke, F.M., Tarasick, D.W., Thompson, A.M., Streets, D.G., Liu, X., 2010. Trans-pacific transport of reactive nitrogen and ozone to Canada during spring. Atmos. Chem. Phys. 10 (17), 8353–8372. https://doi.org/10.5194/acp-10-8353-2010.

Xie, J., Zhu, J., Li, Y., 2008. Assessment and inter-comparison of five high-resolution sea surface temperature products in the shelf and coastal seas around China. Continent. Shelf Res. 28, 1286–1293. https://doi.org/10.1016/j.csr.2008.02.020.

Zhang, L., Chen, Y., Zhao, Y., Henze, D.K., Zhu, L., Song, Y., Paulot, F., Liu, X., Pan, Y., Lin, Y., Huang, B., 2018. Agricultural ammonia emissions in China: reconciling bottom-up and top-down estimates. Atmos. Chem. Phys. 18 (1), 339–355. https://doi.org/10.5194/acp-18-339-2018.

Zhang, Q., Streets, D.G., Carmichael, G.R., He, K.B., Huo, H., Kannari, A., Klimont, Z., Park, I.S., Reddy, S., Fu, J.S., Chen, D., Duan, L., Lei, Y., Wang, L.T., Yao, Z.L., 2009. Asian emissions in 2006 for the NASA INTEX-B mission. Atmos. Chem. Phys. 9 (14), 5131–5153. https://doi.org/10.5194/acp-9-5131-2009.

Zhao, C., Wang, Y., 2009. Assimilated inversion of NO_x emissions over east Asia using OMINO2 column measurements. Geophys. Res. Lett. 36 (6), 1–5. https://doi.org/10.1029/2008GL037123.